Heteroepitaxial van der Waals semiconductor superlattices

Gangtae Jin
Institute for Basic Science
Chang-Soo Lee
Pohang University of Science and Technology (POSTECH)
Odongo Francis Okello
Pohang University of Science and Technology
Suk-Ho Lee
Institute for Basic Science
Min Yeong Park
Institute for Basic Science
Soonyoung Cha
Institute for Basic Science
Seung-Young Seo
Pohang University of Science and Technology (POSTECH)
Gunho Moon
Institute for Basic Science
Dong-Hwan Yang
Pohang Science and Technology University
Cheolhee Han
Pohang University of Science and Technology https://orcid.org/0000-0002-8936-9407
Hyungju Ahn
Pohang University of Science and Technology
Jekwan Lee
Seoul National University
Hyunyong Choi
Seoul National University https://orcid.org/0000-0003-3295-1049
Jonghwan Kim
Pohang University of Science and Technology
Si-Young Choi
Pohang University of Science and Technology (POSTECH) https://orcid.org/0000-0003-1648-142X
Moon-Ho Jo (mhjo@postech.ac.kr)
Institute for Basic Science https://orcid.org/0000-0002-3160-358X

Article

Keywords: epitaxial growth, van der Waals (vdW) semiconductor superlattices (SLs)

Posted Date: February 11th, 2021

DOI: https://doi.org/10.21203/rs.3.rs-193065/v1

Version of Record: A version of this preprint was published at Nature Nanotechnology on July 15th, 2021. See the published version at https://doi.org/10.1038/s41565-021-00942-z.

Abstract

We report atomic layer-by-layer epitaxial growth of van der Waals (*vdW*) semiconductor superlattices (SLs) with programmable stacking periodicities, composed of more than two kinds of dissimilar transition-metal dichalcogenide monolayers (MLs), such as MoS_2, WS_2 and WSe_2. The kinetics-controlled *vdW* epitaxy in the near equilibrium limit by metalorganic chemical vapour depositions enables to achieve accurate ML-by-ML stacking, free of interlayer atomic mixing, resulting in the tunable two-dimensional (2D) *vdW* electronic systems. We identified coherent atomic stacking orders at the *vdW* heterointerfaces, and present scaling valley polarized optical excitations that only pertain to a series of 2D type II band alignments.

Main Text

For decades, semiconductor superlattices (SLs), periodically layered structures of two alternating semiconductors in the atomic thickness regime, have served as the material platform of various heterojunction devices in modern electronics, photonics and display technology[1,2]. Such prominent SL examples can be listed as III-V compound semiconductor SLs (*i.e.*, GaAs/AlGaAs and GaInAs/AlInAs) for high electron mobility transistors[3,4] and quantum cascade lasers[5,6], GaN/AlGaN SLs for light emitting diodes[7,8] and Si/Ge SLs for strained Si CMOS[9]. Therein, the constituent semiconductors are “covalent-bonded” across the heterointerfaces with the lattice-matching coherences[10-12], where the two-dimensional (2D) charge carriers form diverse quantum well (QW) structures, depending on the degrees of interlayer coupling strengths[13]. Meanwhile van der Waals (*vdW*) semiconductors, which often stemmed from transition-metal dichalcogenides (TMDCs, MX_2, where *M* and *X* represent transition-metal ions and chalcogen ions), naturally ensue the inherent 2D confinements within the unit monolayer (ML) across the chemical-bond free *vdW* gaps[14-16]. As a broad range of TMDC semiconductors are available as a ML crystal with diverse electronic structures, precise integration of each kind into *vdW*-SLs can generate another category of the QW structures for unexplored functionalities[17-19]. Despite extensive research on the bilayer stacks of dissimilar *vdW*-MLs to investigate new types of interlayer excitations, such as interlayer excitons[20-23] and twist-angle dependent strong correlations[24,25], little is known for the QW states of *vdW*-SLs [26,27], mainly due to fact that they are not synthetically available to date[28]. Otherwise, they can be prepared by manual transfer-based stacking with some atmospheric impurities, which may not be unavoidable for the scalable integrations[29-31]. In this work, we report direct growth of *vdW*-SLs, heteroepitaxially stacked with MoS_2, WS_2 and WSe_2 MLs, by metalorganic chemical vapour depositions (MOCVD)[32,33]. We have achieved precise ML-by-ML sequential stacking with atomically clean and sharp heterointerfaces by kinetic control of heteronucleation in the near-equilibrium limit[32,34,35]. This ML-by-ML stacking epitaxy also enables to realize the tunable *vdW* SL electronic structures in ML precision. We identified several atomic stacking orders at the *vdW* heterointerfaces, and present scalable valley polarized optical excitations that only pertain to a series of 2D type II band alignments.

Heteroepitaxial growth of *vdW* semiconductor superlattices

Elemental variation in the MX_2 SLs can be achieved either in *M*-alteration ($MX_2/M'X_2$) or *X*-alteration series (MX_2/MX'_2). We demonstrated both series in MoS_2/WS_2 and WS_2/WSe_2 SLs with time-lapse precursor modulations by MOCVD. The first example of MoS_2/WS_2 SLs was discussed in Fig. 1. The predetermined flow rates of $Mo(CO)_6$ and $W(CO)_6$ precursors for each MoS_2 and WS_2 ML were set to 4 sccm and 3 sccm on the $(C_2H_5)_2S$ background flow of 2 sccm in a given growth sequence. A series of cross-sectional high-angle annular dark-field scanning transmission electron microscopy (HAADF-STEM) images in Fig. 1a, taken in each growth step up to 7 ML stacks, demonstrate the precise ML-by-ML stacking of WS_2 and MoS_2. We have successfully achieved such *vdW* stacking epitaxy by the kinetics-controlled growth in the near-equilibrium limit, *i.e.*, the lateral growth rate, n_{growth}, in each ML was ~ 0.15 nm/min to guarantee the full lateral coverage, which is far slower than the cases of ~ 1500 nm/min in the usual thermal CVD growth[33], by setting the lower growth temperatures (550 °C) and precursor partial pressures (~ 10^{-7} torr) of MO precursors. This optimized growth condition essentially suppresses the unwanted overgrowth and interlayer mixing[36,37] - also see Supplementary Figs. 1-4 for the detailed growth optimizations. Here we stress that the basal planes of the first MLs with the highly preferred in-plane orientations are the prerequisite for the ML-by-ML growth. For that, we have grown the first ML films on the step-and-terrace terrains of *c*-sapphire substrates, which were then mechanically transferred on SiO_2/Si substrates as the growth templates for the subsequent stacking growth. We fully discuss these features in Fig. 3. The layered structures of MoS_2/WS_2 SLs in greater details were presented in Fig. 1b, where the total 9 MLs (1:1 alternation of 5 WS_2 MLs and 4 MoS_2 MLs) were captured by the *Z*-contrast in HAADF-STEM image and energy dispersive X-ray spectroscopy (EDX) spectra. One can clearly identify the distinct intensity contrast between WS_2 and MoS_2 MLs, arising from the atomic number (Z) difference of $Z_{Mo} = 42$ and $Z_W = 74$, where the brighter MLs are WS_2 and the darker MLs are MoS_2. In addition, the periodically alternating W-L_a and Mo-K_a peak intensity across each *vdW* gap, assures such SL modulations. Although the image in Fig. 1b cannot be atomically resolved with a fixed TEM zone axis in the entire area, due to finite in-plane orientation variants of each ML, when the zone axis is aligned to <11 0> of the lowest ML, the local atomic structures can be identified in the bright-field (BF) STEM images. For example, we observed either *AC* (translation) or *AA'* (180° rotation) stacking sequences between WS_2 and MoS_2 MLs with the > 90 % area coverage (Fig. 1c) – we call these stacking polytypes “coherent stacks” as classified in Supplementary Fig. 5. We also found local areas with some mixtures of random rotation stacks with the < 10 % area coverage (Fig. 1d) – we call these random orientation stacking polytypes “incoherent stacks”. Interestingly, we found different values of the interlayer distances for coherent and incoherent stacks to be 0.606 nm and 0.647 nm, arising from different *vdW* gap sizes, consistent with the calculations[38]: we also note that the value at the coherent stack, where individual atoms tend to reside at the thermodynamically stable coordinates, is notably smaller than the average value from mechanical stacking cases[39]. The synchrotron grazing incidence wide-angle X-ray diffraction (GI-WAXD) was employed to obtain larger-scale crystallographic coherence in both out-of-plane (*i.e.*, q_z) and in-plane (*i.e.*, q_{xy}) directions of our SLs, as in Fig. 1e. The 2D pattern of GIWAXS at the incidence angle of 0.12° in Fig. 1f shows a series of sharp Bragg spots in reciprocal space, indicating the highly ordered $P6_3/mmc$

structures of our MoS_2/WS_2 SLs (9 ML stacks). For a reference, we compared GI-WAXD patterns from homoepitaxial MoS_2 9L, which possesses smaller grain sizes of ~ 80 to 100 nm in Supplementary Fig. 6. The 1D line-cut profiles were analyzed in both out-of-plane (q_z) and in-plane (q_{xy}) directions, as shown in Fig. 1g,h. The q_z line-cut profile at q_{xy} = 2.3 Å $^{-1}$ clearly shows 4 diffraction peaks from heteroepitaxial MoS_2/WS_2 SLs (purple) and homoepitaxial MoS_2 9Ls (grey), verifying the highly ordered stacking textures – more pronounced peaks from MoS_2/WS_2 SLs indicate the higher degree of ordering, due to larger grain sizes. The interlayer distances are extracted from the (103) diffractions to be 0.616 nm, consistent with the value at the coherent stack regions measured from STEM images. Similarly we find it to be 0.617 nm from MoS_2 9Ls - see also Supplementary Table 1 for the complete diffraction analyses. The vertical coherence length, $L_{c(103)}$, which strictly quantifies the number of coherently repeating layers along the q_z direction, can be also extracted to 1.87 nm by Scherrer equation – it is 1.49 nm in MoS_2 9Ls. The in-plane diffraction peaks of (100), (110), and (200) are also distinct, and much pronounced in MoS_2/WS_2 SLs, suggesting the highly ordered in-plane textures with preferred orientations. Therein we extracted the (100) interplanar distance to be 0.273 nm from the (100) diffractions in the q_{xy} line-cut profiles at q_z = 0 Å $^{-1}$ - see also Supplementary Table 2. Overall, we define the crystalline textures of our *vdW* SLs as largely coherent *vdW* vertical stacks, composed of in-plane oriented polycrystalline MLs.

Designer growth of *vdW* semiconductor superlattices with tunable periodicities

The established heteroepitaxial stacks of MoS_2/WS_2 SLs by a ML-by-ML mode enables to achieve designed SLs with arbitrary periodicities. Figure 2a,b demonstrate 1:2 MoS_2/WS_2 SLs and 2:2 MoS_2/WS_2 SLs. This growth tunability in our *vdW* SL heteroepitaxy is markedly contrasted from previous covalent-bonded SLs, which intrinsically suffer from the strict requirements of lattice matching heteroepitaxy upon stacking. We also show an example of *X*-alteration SLs in MX_2, *i.e.*, WSe_2/WS_2 SLs in Fig. 2c, where we employed $(C_2H_5)_2S$ and $(C_2H_5)_2Se$ precursors in each time-lapse on the continuous $W(CO)_6$ background flow for the WS_2 and WSe_2 MLs (see also Supplementary Fig. 1 and 7 for the growth optimizations). Although the intensity contrast between WS_2 and WSe_2 MLs was less obvious in the *Z*-contrast in HAADF-STEM image, due to smaller Z-sensitivity, compared to MoS_2/WS_2 SLs, the periodic oscillation of S-K_a and Se-K_a peaks in the EDX spectra clearly validates SL modulations. Then, we have successfully established both *M*- and *X*-modulated SLs, heteroepitaxial $WSe_2/MoS_2/WS_2$ trilayers, as shown in Fig. 2d. In addition, our heteroepitaxial growth can be extended to include graphene, which was intermittently inserted by an *ex-situ* dry-transfer method (Fig. 2E and Supplementary Fig. 8).

In-plane crystalline textures of *vdW* semiconductor superlattices

Heteroepitaxial evolution of in-plane crystal textures of our *vdW* SLs are investigated in $WSe_2/WS_2/MoS_2$ trilayers, where the chemical compositions vary for both *M* and *X*, and the in-plane lattice constants also vary - they are known as 0.315 nm for bulk WS_2 and MoS_2, and 0.328 nm for bulk WSe_2[40]. Figure 3a-c are the schematic descriptions of each stacking during the successive growth, in which the initially formed

multiple triangular facet crystals merge to form continuous MLs. Statistical variation in the in-plane crystal orientations can be verified in six-fold periodic clustering of (10 0) diffraction patterns with some degree of angular spreads (inset of Fig. 3d). The first bottom MoS_2 ML was formed by multiple nucleation on the regular step and terrace terrains of *c*-sapphire substrates to initiate the preferred in-plane crystal orientations with a typical grain size of ~ 0.1 to 1 μm, which are either 0° or 60° rotated with respect to each other, as captured by a series of atomic force microscopy (AFM) images in Fig. 3d (see also Supplementary Figs. 9 and 10). This ML-by-ML growth proceeded upon the successive stacking growth for the second (WS_2) (Fig. 3e) and third (WSe_2) (Fig. 3f) MLs with smaller grains of 90 - 100 nm – see also in-plane TEM images in Supplementary Fig. 11 and grain size distribution in Supplementary Fig. 12. The larger lattice parameter of 0.331 nm in the third WSe_2 ML was also verified from the (11 0) diffraction patterns, where we also measured those of underlying MoS_2 and WS_2 to be 0.322 nm (inset of Fig. 3f). Atomic scale images of such in-plane crystalline textures were directly captured by in-plane HAADF-STEM observations of partially covered bilayers, WS_2/MoS_2, as in Fig 3g-k. We verified that the top MLs are preferentially oriented with the basal planes of the bottom MLs, and the stacking polytypes are mostly either AA' (Fig. 3g and Supplementary Fig. 13) or AC coherent stacking (Fig. 3h). Such textures introduce grain boundaries (GBs), mainly identified as 0° or 60° GBs, which were interfaced between either AC-AC domains (Fig. 3k) or AC-AA' domains (Fig. 3j and Supplementary Fig. 14). We also observed random interlayer twists, showing Moiré interference patterns (Fig. 3i). According to first-principles calculations[41], the formation energies of small angle (< 5°) and 60° GBs are relatively smaller than those of random angle GBs, suppressing the unwanted local overgrowth of the second MLs – for example, the second ML preferentially nucleates at the random angle GBs (other than 0° or 60° GBs), leading to non ML-by-ML growth. Whereas on the first MLs with 0° or 60° GBs, the nucleation is not locally concentrated leading to the ML-by-ML growth. We indeed observed such growth patterns, where on the smaller grained MoS_2 ML templates with random GBs, the initial nuclei of the second WS_2 are predominantly populated at such GBs (Supplementary Fig. 3). However, on the larger grained first ML with 0° or 60° GBs, the initial nuclei are uniformly distributed on the entire surfaces. It suggests that the preferred orientation growth in our work is critical to maintain the coherent ML-by-ML growth.

Valley-polarized interlayer excitations in type-II *vdW* superlattices

As for the electronic structures of our *vdW* SLs, we estimate them to be a series of type-II band alignments across the *vdW* gaps to a lowest order. Optical absorption spectra, collected from a series of SLs and each individual MLs in Fig. 4a, one can identify additive features of optical absorption with increasing ML stacks – the spectra of $(MoS_2/WS_2)_n$ SLs, where *n* is the bilayer stack numbers, are linear sums of WS_2 and MoS_2 MLs, according to Voigt fitting (Supplementary Fig. 15) – see also Supplementary Fig. 16 for a series of Raman scattering spectra, obtained from the same SL batches. One of the most distinctive electronic features that only pertain in TMDC ML heterostructures is the large and long-lived spin-valley polarization of charge carriers as observed earlier in (mechanically transferred) WS_2/WSe_2 and WSe_2/MoS_2 bilayers by pump-probe spectroscopy[42]. The ultrafast interlayer charge transfer process across the type-II alignment dramatically suppresses the exciton exchange interaction which is the major

relaxation channel of valley polarization in TMDC MLs. We indeed observed scaling of such temporal population of the valley-polarized carriers, arising from a series of type-II band alignments in our MoS_2/WS_2 SLs. Figure 4b,c illustrate such valley-polarized excitations in real and momentum space with optical circular dichroism (CD), using time-resolved pump-probe spectroscopy. First, the pump pulses with the right-handed circular polarization (σ+) (blue arrows in Fig. 4b,c) creates the valley-polarized excitons on *K* valleys in MoS_2 MLs. Then, the immediate interlayer hole transfer occurs across the type-II alignments from the MoS_2 ML valence bands to that of WS_2 MLs within the ultrafast timescale less than 50 fs[43]. Initially, we verified such interlayer charge separation from the substantially extended lifetime of the CD dynamics in our MoS_2/WS_2 bilayers, compared to that of MoS_2 MLs (see Supplementary Fig. 17). Note that our SL series show shorter lifetime of valley polarization (~nsec), presumably due to higher defect densities, compared to mechanically exfoliated cases. Nevertheless, the valley-polarized electron selectively remains on the *K* valley of MoS_2 MLs (see the upper panel of Fig. 4c). After the pump excitation, the delayed probe pulse (red arrows) was focused on the SLs, and by measuring the pump-induced differential reflectance ΔR with both σ^+ and left-handed (σ^-) circular polarization of the probe beam, we can evaluate CD = $(\Delta R_{\sigma+} - \Delta R_{\sigma-})/R_0$, where R_0 is probe reflectance without the pump. Such valley-polarized electron gives rise to a helicity-dependent absorption difference (*i.e.*, CD). Then, the transient CD response must scale to the amount of the residual valley-polarized electrons in MoS_2 MLs. Figure 4d displays such time-resolved CD responses from a series of $(MoS_2/WS_2)_n$ SLs at 77 K, when the pump and probe photon energy were set to *A*-exciton resonance of MoS_2 MLs with the pump fluence of 5.7 μJ/cm^2. We observed the linearly proportional CD signals with increasing *n* in $(MoS_2/WS_2)_n$ SLs, as in Fig. 4d.

Methods

Growth of the first ML templates with preferred in-plane crystal orientations

MS_2 (*M*: Mo, W) ML templates were epitaxially grown on *c*-plane sapphire substrates. Prior to the MOCVD growth, sapphire substrates were annealed in ambient air at the temperature of 1150 °C for 12 hours in a box furnace, then loaded into our MOCVD system. Pretreatment of *c*-plane sapphire substrates with chalcogen precursors is known to play a role in enhancing the *vdW* epitaxy[44,45]. Thus before the growth, the 2-inch hot-walled quartz tube furnace was ramped up to 650 °C for 40 min, and pretreated for 1 hour with $(C_2H_5)_2S$ under the constant partial pressure of 3.3×10^{-4} torr, and the carrier gas flow of 150 standard cubic centimeters per minutes (sccm) for Ar (99.9999 %) and 1 sccm for H_2 (99.9999 %) at total pressure of 4 torr. After the sulfur treatment, the furnace was ramped up to the growth temperature of 750 °C for 10 min. The total pressure was kept at 1.9 torr under the carrier gas flow of 250 sccm for Ar and 5 sccm for H_2. Eutectic salts of KCl and KI was placed at the upstream region of the quartz tube. The growth of MoS_2 on sapphire substrates was conducted for 32 hours. During the growth, $Mo(CO)_6$ and $(C_2H_5)_2S$ were supplied under the constant partial pressure of 1×10^{-6} torr and 1×10^{-4} torr respectively. Both precursors were kept in bubbler-typed canisters at a constant pressure of 1050 torr with Ar, and

maintained at a constant temperature of 10 ^{o}C for $Mo(CO)_6$ and room temperature (RT) for $(C_2H_5)_2S$. In the growth of WS_2 on *c*-sapphire substrates (growth time ~ 21 hours), $W(CO)_6$ and $(C_2H_5)_2S$ were supplied under the constant partial pressure of 4×10^{-8} torr and 1×10^{-4} torr, respectively. Both precursors were kept in canisters at a constant pressure of 1200 torr with Ar and maintained at a constant temperature of 0 °C for both $W(CO)_6$ and $(C_2H_5)_2S$. Epitaxial MoS_2 and WS_2 ML templates on *c*-sapphire were spin-coated by poly(methyl methacrylate) (PMMA), then transferred onto fresh SiO_2/p^+-Si substrates using 5% HF solution. PMMA layer was removed by thermal annealing at 350 °C for 2 hours in an ultra-high vacuum chamber (base pressure < 1×10^{-5} torr).

Heteroepitaxy of MoS_2/WS_2 and WS_2/WSe_2 *vdW* SLs

Epitaxial MoS_2/WS_2 SLs were grown on either MoS_2 or MoS_2 ML templates. The 2-inch hot-walled quartz tube furnace was ramped up to 550 °C for 30 min and the total pressure was kept at 1.9 torr under the carrier gas flow of 150 sccm for Ar and 2 sccm for H_2. KCl/KI crucible was placed at the upstream region of the quartz tube. The growth time of MoS_2/WS_2 SLs was determined by the number of layers and sequences, *i.e.*, 70 hours (2L), 48 hours (4L), 47 hours (6L), and 46 hours (8L) for MoS_2, 24 hours (3L), 23 hours (5L), 22 hours (7L), and 21 hours (9L) for WS_2. During the given growth time, $(C_2H_5)_2S$ was constantly supplied under the constant partial pressure of 1.5×10^{-3} torr. Meanwhile, $Mo(CO)_6$ (partial pressure of ~ 1×10^{-6} torr) and $W(CO)_6$ (partial pressure of ~ 5.8×10^{-8} torr) were alternated for a given growth time per 1L with breaks for 20 minutes to purge out the residual precursors in the chambers and to adjust the temperature of precursors between each alternation (10 °C for $Mo(CO)_6$ and 0 °C for $W(CO)_6$). Epitaxial WSe_2/WS_2 SLs were also grown on the ML templates. The 2-inch hot-walled quartz tube furnace was ramped up to 550 °C for 30 min and the total pressure was kept at 1.9 torr under the carrier gas flow of 200 sccm for Ar 7.5 sccm for H_2. KCl/KI was placed at the upstream region of the quartz tube. The growth time of WSe_2/WS_2 SLs was determined by the number of layers and sequences, *i.e.*, 38 hours (2L), 27 hours (4L), and 26 hours (6L) for WSe_2 and 25 hours (3L) and 24 hours (5L) for WS_2. During the given growth time, $W(CO)_6$ was constantly supplied under the constant partial pressure of 3×10^{-8} torr. Meanwhile, $(C_2H_5)_2S$ (partial pressure of 1.3×10^{-3} torr) and $(CH_3)_2Se$ (partial pressure of 2.4×10^{-3} torr) were alternated for a given growth time per 1L with long breaks that conducted by ramping down the furnace temperature to room temperature and ramping up the furnace up to 550 °C for 1 hour. All precursors were kept in bubbler-typed canisters at a constant pressure of 1100 torr with Ar and maintained at a constant temperature of -1 °C for $W(CO)_6$ and RT for $(C_2H_5)_2S$ and $(CH_3)_2Se$.

Synchrotron grazing incidence wide angle X-ray diffraction (GI-WAXD)

The synchrotron GI-WAXD measurements were performed at the 9A U-SAXS beamline of the Pohang Light Source-II. The X-ray from the in-vacuum undulator is monochromated using Si (111) double crystals and focused at the detector position using K-B type mirror. The 2D GI-WAXD patterns were recorded on a 2D CCD (Rayonix MX170-HS). The incidence angles, wavelength of X-ray, sample-to-detector distance, and

exposure time were set to be 0.12°, 0.623 Å (energy = 19.795 keV), 220.242 mm, and 3s, respectively. To denote the index (*hkl*) and the interplanar distance (*d*) of the specific plane, we assumed that the space group of our *vdW* SLs is $P6_3/mmc$, which corresponds to 2H-phase TMDCs (AA' stacks).

Optical absorption measurements

Optical absorption measurements of MoS_2/WS_2 SLs were conducted by PerkinElmer-LAMBDA 950 UV-Vis-NIR spectrophotometer with transmission mode. A series of $(MoS_2/WS_2)_n$ SLs (*n* is the bilayer stack numbers), and each individual MLs are transferred on double-side polished sapphire wafers using PMMA-supported wet-transfer methods, and PMMA is removed by high vacuum annealing at 350 °C for 3 hours. The absorption was calculated from the following equations under thin film approximation.

$$A = \frac{n_{substrate} + 1}{2} \times \frac{T_{substrate} - T_{SLs}}{T_{substrate}}$$

, where *A* is the absorption of the sample, $n_{substrate}$ is the refractive index of sapphire substrate, *T* is the transmittance of the bare sapphire substrate and the SLs[46].

Transmission electronic microscope (TEM) analyses

For plan-view TEM observations, TMDC SLs are transferred on Cu TEM grids (holey carbon film grids for DF-TEM imaging and quantifoil grids for STEM analyses) using PMMA assisted wet-transfer methods. Specimens for the cross-section TEM observations were prepared by a focus ion beam (Helios Nanolab 650, FEI). For the protection, 50-nm thickness amorphous carbon layer was deposited on top of the specimen using a carbon evaporator. In the Fig. 1d, 1e, and 3d-h, imaging was conducted by JEOL JEM-ARM 200F with a C_s-corrected probe operated at 80 kV. The rest of STEM imaging, DF-TEM imaging, and SAED patterns were performed by using a JEOL 2100F with the C_s-corrected probe operated at 200 kV. EDX was conducted by X-Max EDX systems (Oxford Instrument). Characteristic Mo-K_α, W-L_α, S-K_α, Se-K_α, and C-K_α X-ray signals were used in the EDX line-profiles.

Time-resolved pump-probe spectroscopy for valley polarized carrier dynamics study

As-grown MoS_2/WS_2 SLs on SiO_2/p^+-Si substrates were spin-coated by PMMA, then transferred onto fresh sapphire substrates using water-assisted transfer. PMMA layer was removed by thermal annealing at 350 °C for 2 hours in an ultra-high vacuum chamber (base pressure < 1×10^{-5} torr). To investigate ultrafast valley-polarized carrier dynamics in our $(MoS_2/WS_2)_n$ SLs, time-resolved pump-probe spectroscopy was employed. The output of femtosecond laser source (PHAROS, Light Conversion) and optical parametric amplifier (ORPHEUS) serves wavelength-tunable pump and probe pulses with a repetition rate of 100 kHz and a pulse duration of 50 fs and spectral bandwidth of 50 meV. Both pulses were simultaneously focused on the samples using an objective lens (X40, NA = 0.5), whose relative delay was controlled by a motorized translational stage. The pump pulses were modulated by the optical

chopper, and the change in the probe reflection is recorded by a photomultiplier tube connected to the current amplifier and lock-in amplifier. The optical polarization of both pulses was manipulated independently by quarter wave plates.

Declarations

Data and materials availability: All data needed to evaluate the conclusions in the paper are present in the paper and/or the Supplementary Materials. Additional data related to this paper may be requested from the authors.

Contributions:

G.J., C.-S.L., and M.-H.J. conceived and designed the project. G.J., C.-S.L., S.-H.L., and M.Y.P. conducted MOCVD growth experiments and material characterizations. O.F.N.O., D.H.Y., and S.-Y.C. performed the TEM measurements and analyzed the data. S.-Y.S and G.M. fabricated the devices and performed optical measurements. S.C., C.H., J.L., J.K., and H.C. carried out ultrafast laser spectroscopy. G.J., C.-S.L., S.C., and M.-H.J. wrote the paper. M.-H.J. supervised the project. All the authors discussed the results and commented on the manuscript.

Corresponding author

Correspondence to Moon-Ho Jo

Competing interests:

The authors declare no competing interests.

Acknowledgement:

This work was supported by the Institute for Basic Science (IBS), Korea under Project Code IBS-R014-A1.

References

1. . Ando, T., Fowler, B., & F. Stern, Electronic properties of two-dimensional systems, *Rev. Mod. Phys*. **54**, 437-672 (1982).
2. Anderson, D.A. & Apsley, N. Electronics: Semiconductor superlattices *Nature*, **305**, 668-669 (1983).
3. Dingle, R., Störmer, H. L., Gossard, A. C., & Wiegmann, W. Electron mobilities in modulation-doped semiconductor heterojunction superlattices. *Appl. Phys. Lett.* **33**, 665–667 (1978).
4. Mimura, T., Hiyamizu, S., Fujii, T., & Nanbu, K. A New Field-Effect Transistor with Selectively Doped GaAs/n-$Al_xGa_{1-x}As$ Heterojunctions. *Jpn. J. Appl. Phys.* **19**, L225-L227 (1980).
5. Faist, J. et al. Quantum cascade laser. *Science* **264**, 553–556 (1994).
6. Köhler, R. et al. Terahertz semiconductor-heterostructure laser. *Nature* **417**, 156-159 (2002).

7. Nakamura, S. The roles of structural imperfections in InGaN-based blue light-emitting diodes and laser diodes. *Science* **281**, 956–961 (1998).
8. Khan, A., Balakrishnan, K., & Katona, T. Ultraviolet light-emitting diodes based on group three nitrides. *Nat. Photonics* **2**, 77-84 (2008).
9. Abstreiter, G., Brugger, H., Wolf, T., Jorke, H., & Herzog, H. J. Strain-Induced Two-Dimensional Electron Gas in Selectively Doped Si/Si_xGe_{1-x} Superlattices. *Phys. Rev. Lett.* **54**, 2441-2444 (1985).
10. Zur, A. & McGuill, T. C. Lattice match: An application to heteroepitaxy, *J. Appl. Phys.* **55**, 378-386 (1984).
11. Bauer, E. & van der Merwe, J. H. Structure and growth of crystalline superlattices: From monolayer to superlattice. *Phys. Rev. B.* **33**, 3657-3671 (1986).
12. Bae, S. H. et al. Graphene-assisted spontaneous relaxation towards dislocation-free heteroepitaxy. *Nat. Nanotechnol.* **15**, 272–276 (2020).
13. Mendez, E. E. & Bastard, G. Wannier-Stark Ladders and Bloch Oscillations in Superlattices. *Phys. Today* **46**, 34–42 (1993).
14. Mak, K. F., Lee, C., Hone, J., Shan, J., & Heinz, T. F. Atomically thin MoS□: A new direct-gap semiconductor. *Phys. Rev. Lett.* **105**, 136805 (2010).
15. Radisavljevic, B., Radenovic, A., Brivio, J., Giacometti, V., & Kis, A. Single-layer MoS_2 transistors, *Nat. Nanotechnol*. **6**, 147-150 (2011).
16. Britnell, L. et al. Strong light-matter interactions in heterostructures of atomically thin films. *Science* **340**, 1311–1314 (2013).
17. Chhowalla, M. et al., The chemistry of two-dimensional layered transition metal dichalcogenide nanosheets. *Nat. Chem.* **5**, 263–275 (2013).
18. Geim, A. K. & Grigorieva, I. V. Van der Waals heterostructures. *Nature* **499**, 419-425 (2013).
19. Novoselov, K. S., Mishchenko, A., Carvalho, A., & Castro Neto, A. H. 2D materials and van der Waals heterostructures. *Science* **353**, aac9439 (2016).
20. Yu, H., Wang, Y., Tong, Q., Xu, X., & Yao, W. Anomalous light cones and valley optical selection rules of interlayer excitons in twisted heterobilayers. *Phys. Rev. Lett.* **115**, 187002 (2015).
21. Tran, K. et al. Evidence for moiré excitons in van der Waals heterostructures. *Nature* **567**, 71–75 (2019).
22. Jauregui, L. A. et al. Electrical control of interlayer exciton dynamics in atomically thin heterostructures, *Science* **366**, 870-875 (2019).
23. Heo, H. et al. Interlayer orientation-dependent light absorption and emission in monolayer semiconductor stacks. *Nat. Commun.* **6**, 7372 (2015).
24. Cao, Y. et al. Unconventional superconductivity in magic-angle graphene superlattices. *Nature* **556**, 43–50 (2018).
25. Cao, Y. et al. Correlated insulator behaviour at half-filling in magic-angle graphene superlattices. *Nature* **556**, 80–84 (2018).

26. Schmidt, P. et al. Nano-imaging of intersubband transitions in van der Waals quantum wells. *Nat. Nanotechnol*. **13**, 1035–1041 (2018).
27. Zultak, J. et al. Ultra-thin van der Waals crystals as semiconductor quantum wells. *Nat. Commun.* **11**, 125 (2020).
28. Li, J. et al. General synthesis of two-dimensional van der Waals heterostructure arrays. *Nature*. **579**, 368–374 (2020).
29. Kretinin, A. V. et al. Electronic properties of graphene encapsulated with different two-dimensional atomic crystals. *Nano Lett.* **14**, 3270–3276 (2014).
30. Haigh, S. J. et al. Cross-sectional imaging of individual layers and buried interfaces of graphene-based heterostructures and superlattices. *Nat. Mater.* **11**, 764–767 (2012).
31. Kang, K. et al. Layer-by-layer assembly of two-dimensional materials into wafer-scale heterostructures. *Nature*. **550**, 229–233 (2017).
32. Kang, K. et al. High-mobility three-atom-thick semiconducting films with wafer-scale homogeneity. *Nature* **520**, 656–660 (2015).
33. Jin, G. et al. Atomically thin three-dimensional membranes of van der Waals semiconductors by wafer-scale growth. *Sci. Adv.* **5**, eaaw3180 (2019).
34. Zhang, Z. & Lagally, M. G. Atomistic processes in the early stages of thin-film growth. *Science***276**, 377–383 (1997).
35. Xie, S. et al. Coherent, atomically thin transition-metal dichalcogenide superlattices with engineered strain. *Science* **359**, 1131–1136 (2018).
36. Lu, A.-Y. et al. Janus monolayers of transition metal dichalcogenides. *Nat. Nanotechnol.* **12**, 744–749 (2017).
37. Lee, C.-S. et al. Programmed band gap modulation within van der Waals semiconductor monolayers by metalorganic vapor-phase epitaxy. *Chem. Mater.* **32**, 5084–5090 (2020).
38. Liu, K. et al. Evolution of interlayer coupling in twisted molybdenum disulfide bilayers. *Nat. Commun.* **5**, 4966 (2014).
39. Vaziri, S. et al. Ultrahigh thermal isolation across heterogeneously layered two-dimensional materials. *Sci. Adv.* **5**, eaax1325 (2019).
40. Schutte, W. J., De Boer, J. L., & Jellinek, F. Crystal structures of tungsten disulfide and diselenide. *J. Solid State Chem.* **70**, 207-209 (1987).
41. Zou, X., Liu, Y., & Yakobson, B. I. Predicting Dislocations and Grain Boundaries in Two-Dimensional Metal-Disulfides from the First Principles. *Nano Lett.* **13**, 253-258 (2013).
42. Kim, J. et al. Observation of ultralong valley lifetime in WSe_2/MoS_2 heterostructures. *Sci. Adv.* **3**, e1700518 (2017).
43. Hong, X. et al. Ultrafast charge transfer in atomically thin MoS_2/WS_2 heterostructures. *Nat. Nanotechnol.* **9**, 682–686 (2014).

44. Koma, A. Van der Waals epitaxy for highly lattice-mismatched systems. *J. Cryst. Growth*, **201/202**, 236-241 (1999).
45. Lin, Y.-C. et al. Realizing Large-Scale, Electronic-Grade Two Dimensional Semiconductors. *ACS Nano*, **12**, 965-975 (2018).
46. Mak, K. F. et al. Measurement of the optical conductivity of graphene. *Phys. Rev. Lett.* **101**, 196405 (2008).

Figures

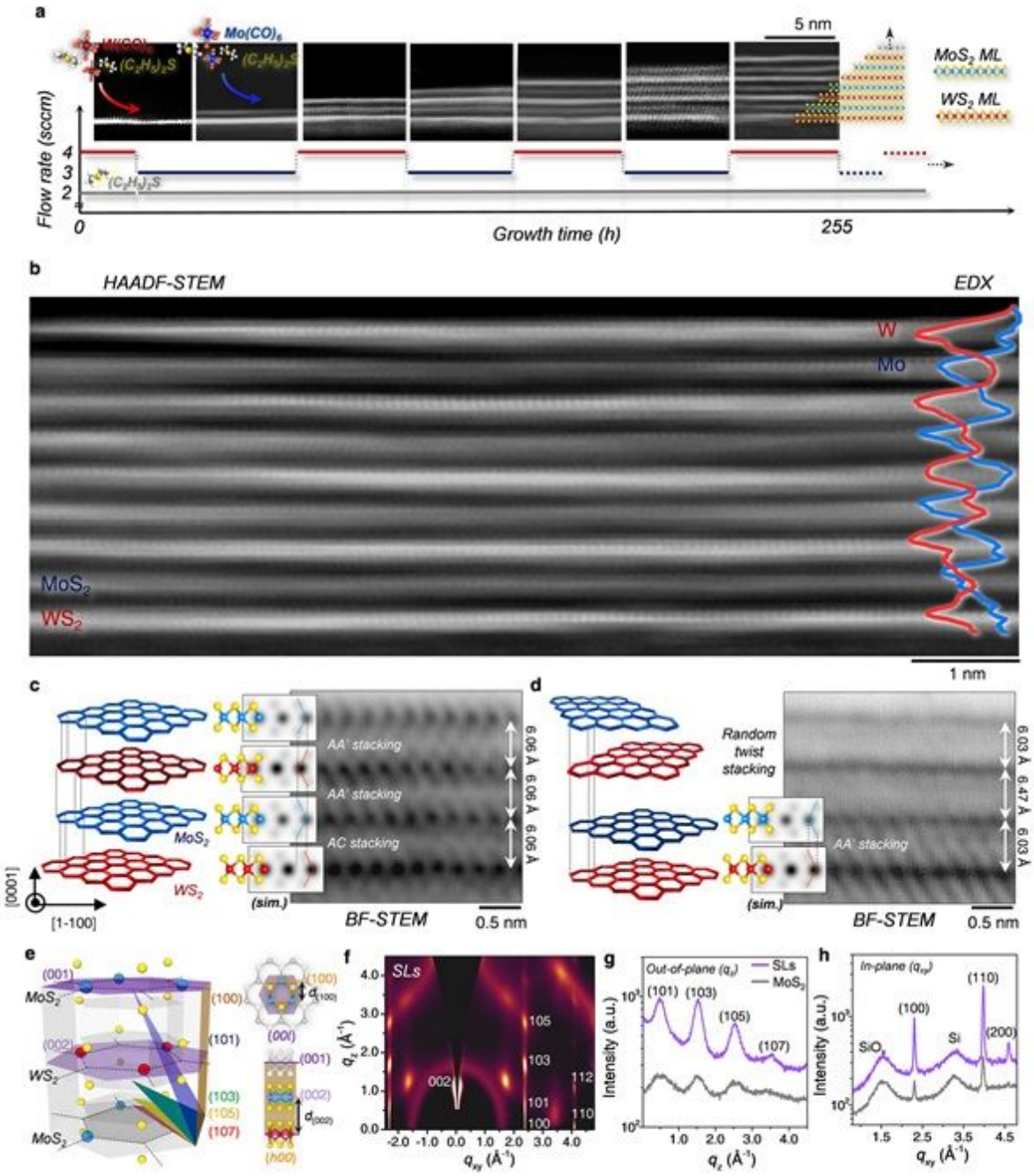

Figure 1

ML-by-ML vdW heteroepitaxy of MoS2/WS2 SLs. a, Flow rate modulations of MO precursors for the growth of MoS2/WS2 SLs and a series of cross-sectional HAADF-STEM images of MoS2/WS2 SLs from 1 to 7 ML stacks. b, Cross-sectional HAADF-STEM images of MoS2/WS2 SLs with the EDX spectra for W-Lα (red) and Mo-Kα (blue) edges. c,d, Schematics (left) and BF-STEM images (right) with the corresponding atomic model simulations for coherent SL stacks (c) and incoherent stack (d). e, Illustration of atomic crystallographic planes of SLs. f, 2D GI-WAXD pattern of MoS2/WS2 SLs (9 ML stacks). g,h, 1D line-cut profiles along the out-of-plane (qz) direction (g) and the in-plane (qxy) direction (h) obtained from MoS2/WS2 SLs and MoS2 9L.

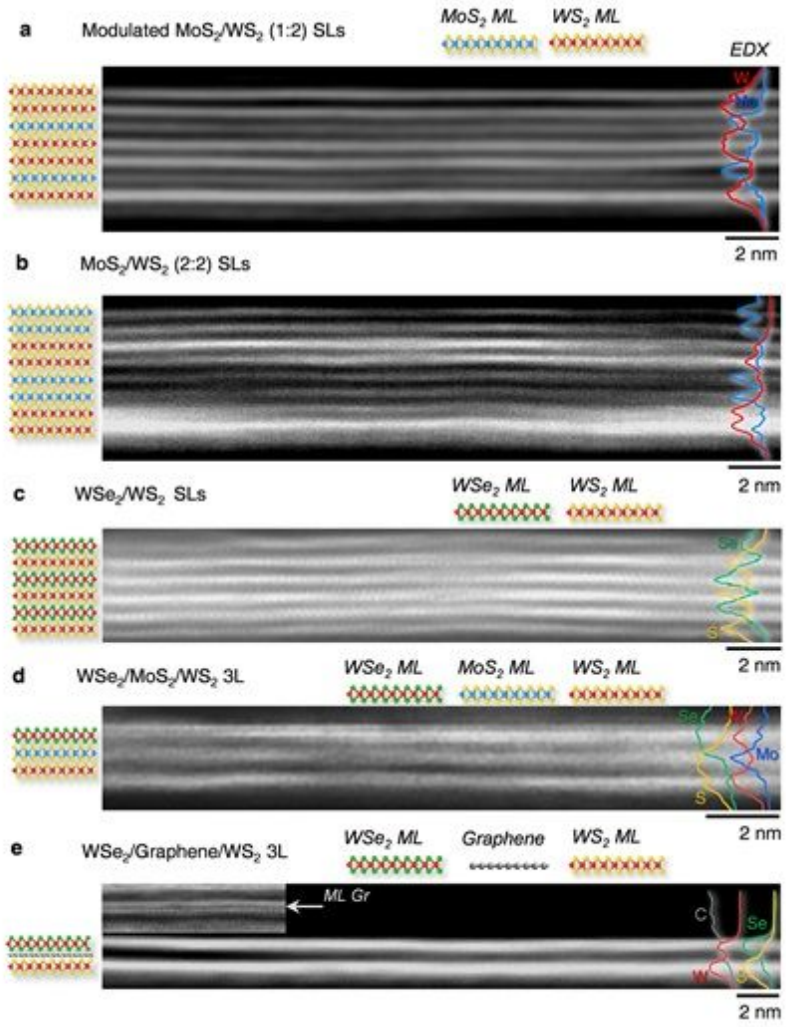

Figure 2

Designer heteroepitaxy of vdW SLs with tunable periodicities. a-e, Cross-sectional HAADF-STEM images with the EDX spectra for Mo-Kα, W-Lα, S-Kα, Se-Kα, and C-Kα edges from MoS2/WS2 SLs with 1:2 periodicity (7 ML stacks) (a), MoS2/WS2 SLs with 2:2 periodicity (8 ML stacks) (b), WSe2/WS2 SLs (6 ML stacks) (c), WSe2/MoS2/WS2 trilayers (d), and WSe2/Graphene/WS2 trilayers (e). Inset of e: BF-STEM image of WSe2/Graphene/WS2 trilayers.

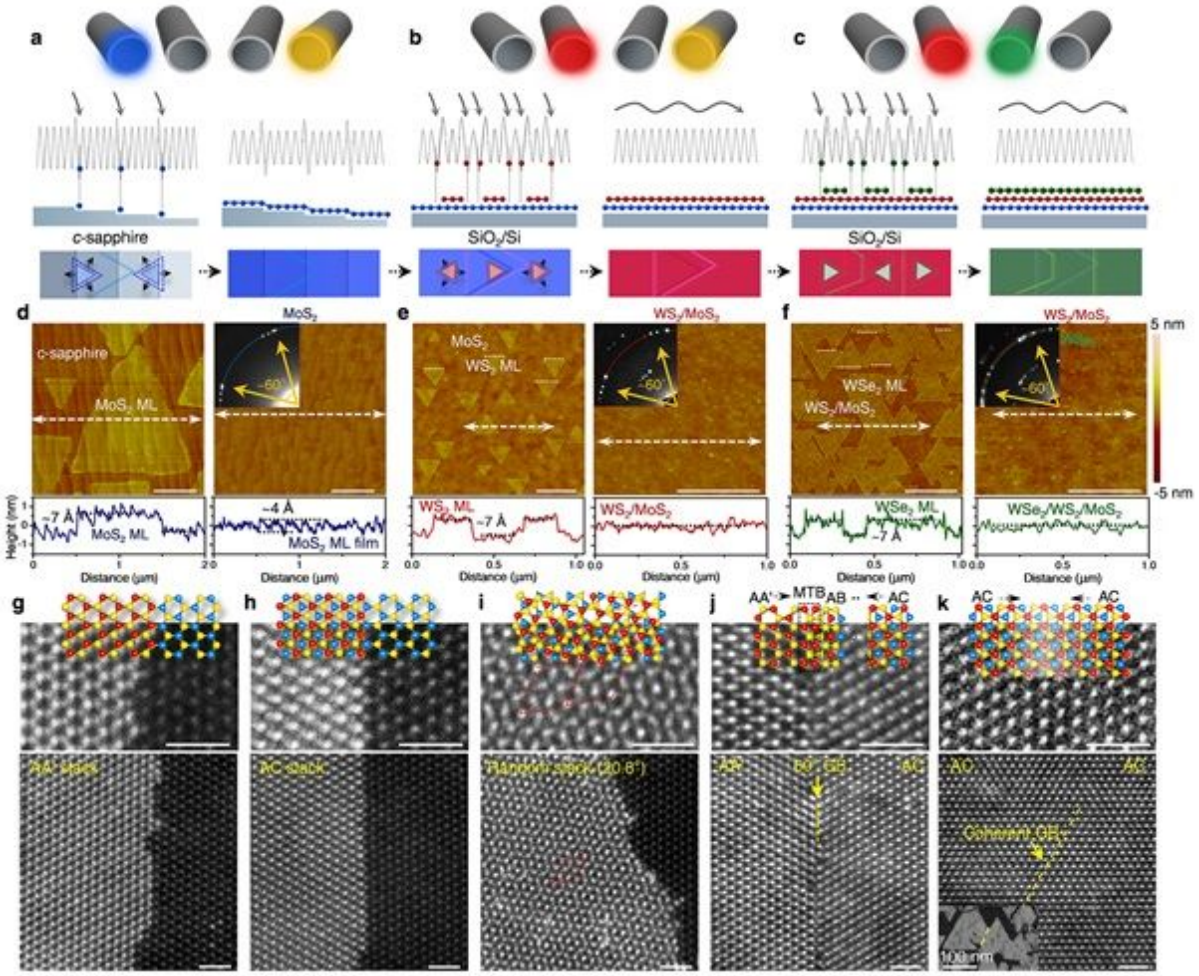

Figure 3

Heteroepitaxial evolution of in-plane crystalline textures of WSe2/WS2/MoS2 trilayers. a-c, Schematics of MO precursor feeds (top), thermodynamic energy landscapes for adatoms (middle), and ML-by-ML epitaxial growth models (bottom) for the first MoS2 ML films (a), the second WS2 ML films (on MoS2) (b), and the third WSe2 ML films (on WS2/MoS2) (c). d-f, A series of AFM images and height profiles along the dashed line for partially covered and fully covered MoS2 ML on c-sapphire (d), WS2 ML on MoS2 (e), and WSe2 ML on WS2/MoS2 bilayer (f). Scale bars, 0.5 μm. Inset: the representative selected area electron diffraction (SAED) patterns. g-k, In-plane HAADF-STEM images with the corresponding atomic models obtained from WS2/MoS2 bilayer at the regions of AA' stack (g), AC stack (h), and incoherent stack (i) and interfaces between AA'-AC domains (j) and AA'-AA' domains (k). Scale bars, 1 nm.

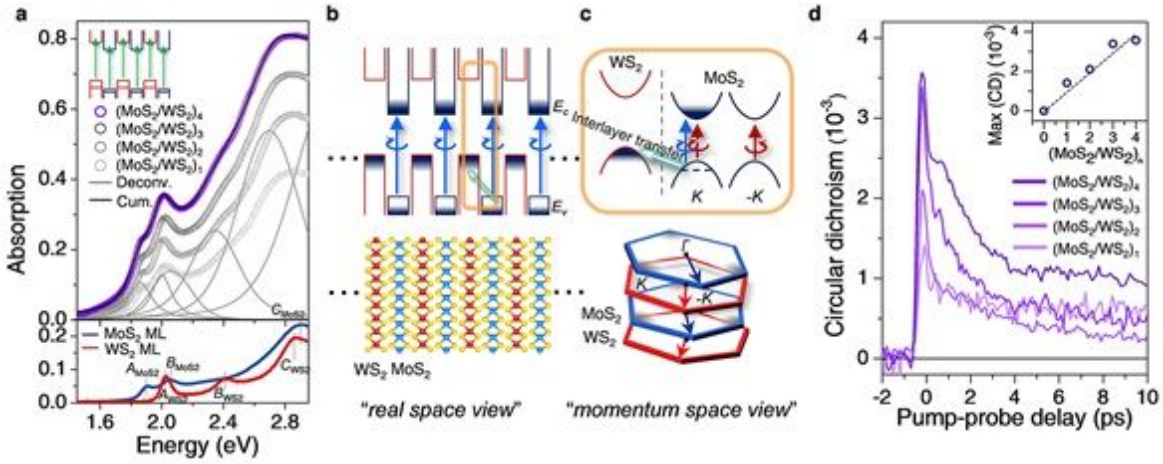

Figure 4

Valley-polarized interlayer excitations in the type-II MoS2/WS2 SLs. a, Optical absorption spectra collected from a series of (MoS2/WS2)n SLs (purple circle for n = 4 and grey circle for n = 1-3), MoS2 MLs (blue), and WS2 MLs (red) with the Voigt fits (gray) and the cumulative fit (black) for (MoS2/WS2)4 SLs. b,c, Illustrations of valley-polarized excitations with the optical CD in real space (b) and momentum space (c). d, Time-resolved CD responses obtained from a series of (MoS2/WS2)n SLs.

Supplementary Files

This is a list of supplementary files associated with this preprint. Click to download.

- vdWSLSI.docx